



Cite this: *Catal. Sci. Technol.*, 2019,  
9, 3373

# Structure-retentive synthesis of a highly ordered mesoporous Nb<sub>2</sub>O<sub>5</sub>/N-doped graphene nanocomposite with superior interfacial contacts and improved visible-light photocatalysis†

Hui Huang, <sup>a</sup> Jun Zhou, <sup>a</sup> Jie Zhou<sup>a</sup> and Mingshan Zhu <sup>\*b</sup>

Owing to their unique chemical and structural properties, highly ordered mesoporous structures are expected to be one of the most promising functional materials for catalysis. In this paper, highly ordered mesoporous niobium pentoxide (MNb) arrayed on N-doped graphene (MNb-NGR) was facilely prepared. The data showed the MNb-NGR composites displaying broad light harvesting in the visible-light region and superior performance for water splitting and resulting in hydrogen (H<sub>2</sub>) production. Under 5 h visible light illumination, the amount of H<sub>2</sub> evolved using the optimized photocatalyst reached 121.1 μmol g<sup>-1</sup>, which was 7.8 times that when using MNb. The improvement in the photocatalytic performance indicated that the hierarchical structure and synergistic effects of MNb and NGR, as well as nitrogen richness of the NGR, were beneficial for promoting charge separation. The study highlights the potential applications of highly ordered mesoporous structure configurations containing N-doped graphene in visible-light photocatalytic systems.

Received 21st March 2019,  
Accepted 31st May 2019

DOI: 10.1039/c9cy00555b

rsc.li/catalysis

## 1. Introduction

Materials having ordered mesoporous structures have received particular interest since the development of ordered mesoporous silicas.<sup>1,2</sup> This interest is due to their intrinsic attractive properties, including nanosized walls, high surface areas, periodically arranged monodispersed mesopore space, uniform nanosized frameworks and tunable pore sizes.<sup>3–6</sup> These unique properties endow ordered mesoporous materials with great advantages in heterogeneous catalytic processes.<sup>7–9</sup> First, the catalytic reaction sites are related to the high surface area, which benefits interface-related processes such as absorption and desorption. Second, the tunable and uniform pores afford nano-effects (surface and quantum effects), endowing the materials with better performance.<sup>3</sup> For instance, the Zhao group reported ordered mesoporous black TiO<sub>2</sub> as a highly efficient hydrogen (H<sub>2</sub>) production photocatalyst. This highly ordered structure was reported to exhibit an activity level twice that of pristine mesoporous TiO<sub>2</sub>.<sup>9</sup>

Of the ordered mesoporous structures of metal oxides, niobium pentoxide (Nb<sub>2</sub>O<sub>5</sub>) has received great attention owing to its low cost and broad applications.<sup>10–18</sup> Moreover, similar to TiO<sub>2</sub>, Nb<sub>2</sub>O<sub>5</sub> also can act as an efficient photocatalyst in various photocatalytic applications. For example, the Prado<sup>10</sup> and Yu<sup>11</sup> groups reported that the Nb<sub>2</sub>O<sub>5</sub> nanostructures worked as photocatalysts for photodegradation of indigo carmine and H<sub>2</sub> production, respectively. However, two issues still need to be addressed before extending the use of Nb<sub>2</sub>O<sub>5</sub> to additional applications. First, its wide bandgap energy of 3.4 eV restricts its activity to just the UV region.<sup>16</sup> Second, the advantages of the highly ordered mesoporous structures of Nb<sub>2</sub>O<sub>5</sub> should be expressed in the photocatalytic process.<sup>17–19</sup>

Hence, we developed a facile route to meet the above demands by combining the highly ordered mesoporous Nb<sub>2</sub>O<sub>5</sub> (MNb) nanostructure with the use of two-dimensional N-doped graphene (NGR). First, Nb<sub>2</sub>O<sub>5</sub> modified by carbon nanostructures has been shown to exhibit good visible-light photocatalytic activity for the degradation of dyes and production of H<sub>2</sub>.<sup>20</sup> Inspired by this attribute, NGR was introduced to improve the light-harvesting ability of the catalyst. Moreover, the NGR not only provided a particularly effective way for extending the range of light absorption but also accelerated the photogenerated electron–hole pair separation, thus improving the efficiency of the photocatalytic activities.<sup>21,22</sup> By combining such a highly ordered mesoporous Nb<sub>2</sub>O<sub>5</sub> nanostructure with nitrogen-doped graphene to form the

<sup>a</sup> Department of Chemistry, Nantong Vocational University, Nantong 226007, P.R. China

<sup>b</sup> School of Environment, Jinan University, Guangzhou 510632, P.R. China.

E-mail: mingshanzhu@yahoo.com, zhumingshan@jnu.edu.cn

† Electronic supplementary information (ESI) available: Additional morphology characterizations. See DOI: 10.1039/c9cy00555b

MNb–NGR hybrid, these two moieties of the composite exhibited a good interfacial connection and the NGR worked as an electron collector and transporter, which synergistically improved electron transport from MNb to NGR nanosheets and restrained recombination of photoelectrons and holes in the MNb.<sup>23–29</sup> The as-prepared MNb/NGR showed a much better photocatalytic performance towards splitting of water and resulting production of H<sub>2</sub> under irradiation with visible light and solar light than did pure Nb<sub>2</sub>O<sub>5</sub> and MNb. The present work provided a potential application of ordered mesostructured Nb<sub>2</sub>O<sub>5</sub> anchored on N-doped graphene as an effective visible-light photocatalyst for conversion of solar energy.

## 2. Results and discussion

The crystalline phases and structures of the samples were investigated by both small-angle X-ray scattering (SAXS) and powder X-ray diffraction (XRD). The results are shown in Fig. 1a. For the MNb sample, two main peaks were observed, at 1.24 and 2.04° and indexed as the (100) and (110) reflections in MNb, indicating a highly ordered mesoporous structure and the presence of long-range ordered mesochannels in our sample.<sup>30–32</sup> Introduction of NGR to form MNb–NGR-5 resulted in a slight shift of the diffraction peaks to 1.26 and 2.06°. These peak shifts in the XRD patterns may have been due to interactions between the MNb and NGR. Moreover, in the wide-angle XRD pattern (Fig. 1a, inset), the MNb showed a distinct diffraction peak centered at 25° and another centered at 55°, indicating that MNb was well crystallized. Moreover, the XRD pattern of the MNb–NGR-5 sample was similar to that of MNb, but no NGR diffraction peaks were found. This result was due to the low content and relatively low diffraction intensity of NGR.<sup>14,30,33</sup>

Raman spectra of MNb, MNb–NGR-5 and NGR samples were acquired, and are shown in Fig. 1b. The NGR sample yielded two strong peaks, at 1351.4 cm<sup>-1</sup> and 1581.1 cm<sup>-1</sup>, which were attributed to the D and G bands of graphene.<sup>32,34</sup> The MNb sample also yielded two prominent bands, here at ca. 217.1 and 676.3 cm<sup>-1</sup>, which corresponded to, respectively, the D and G bands of Nb<sub>2</sub>O<sub>5</sub>.<sup>35,36</sup> And the MNb–NGR-5 composite yielded all of the peaks of graphene and MNb, suggesting the successful formation of a hybrid of MNb and NGR. Compared with NGR, the MNb–NGR-5 showed a stron-

ger D band peak at 1354.7 cm<sup>-1</sup>, which can be attributed to the presence of defects caused by N-doping in the graphene. Furthermore, the G band of the MNb–NGR-5 sample shifted to 1584.3 cm<sup>-1</sup>, further confirming the effect of nitrogen doping. This was the first indication that MNb and NGR combined well in the MNb–NGR composite.

The BET specific surface area and pore diameter of MNb and MNb–NGR-5 were studied by carrying out N<sub>2</sub> adsorption-desorption experiments, as shown in Fig. 2. The N<sub>2</sub> adsorption-desorption isotherms of the MNb and MNb–NGR-5 samples (Fig. 2a) showed that ordered mesoporosity was the basic feature of the as-prepared samples. This result indicated a lack of any significant change in the MNb lattice resulting from introducing NGR. Furthermore, inspection of the pore size distributions indicated that all of these mesoporous samples were made up of 7.5 nm-diameter pore channels (Fig. 2b). The BET specific surface areas and average pore diameters of all samples are summarized in Table 1. The pristine MNb had a uniform pore diameter of 7.456 nm and BET specific surface area of 226.2 m<sup>2</sup> g<sup>-1</sup>. Introducing NGR to form MNb–NGR-5 resulted in an increase in the BET specific surface area to 251.7 m<sup>2</sup> g<sup>-1</sup> and of the pore diameter (*D*<sub>B<sub>JH</sub></sub>) to ca. 7.542 nm. These observations indicated that the pore volume increased slightly with increasing NGR content, and that the initial mesoporous structure of MNb was inherited after NGR was incorporated.

To provide information about the fine structure of the pores, TEM and HRTEM images of samples were acquired. Fig. 3a shows a longitudinal cross-section of the MNb sample. Inspection of this image showed the ordered arrangement of mesopores, with the cylindrical pore channels aligned along [001] and the highly ordered hexagonal arrangement of mesopores along [110]. The view of sample in the image of Fig. 3b showed the hexagonal symmetry of the MNb pore structure, an observation consistent with the XRD results.<sup>37</sup> As shown in Fig. S1,† the two-dimensional structure of NGR sheets with obvious wrinkles hybridized with MNb. Fig. 3c and d show TEM images of MNb–NGR-5. Inspection of this image showed that introducing NGR to MNb did not change the structure of MNb, consistent with the above-described results. In addition, the electron diffraction pattern of the MNb–NGR-5 samples also showed them to be a highly ordered crystalline form of MNb. Moreover, these techniques indicated that the average pore diameter was about 7.5 nm,

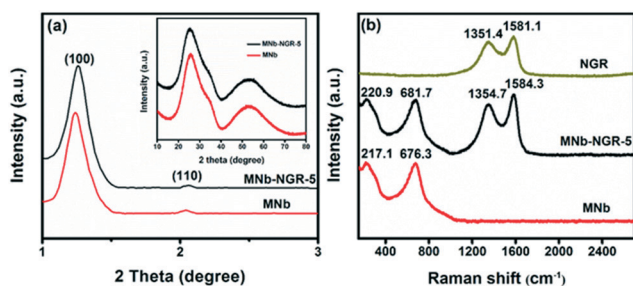


Fig. 1 (a) SAXS and wide-angle XRD (inset) patterns of MNb and MNb–NGR-5. (b) Raman spectra of NGR, MNb and the MNb–NGR-5 composite.

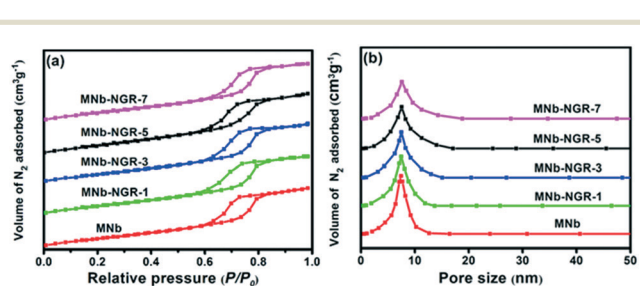


Fig. 2 (a) N<sub>2</sub> adsorption-desorption isotherms and (b) pore diameter distribution curves of MNb and MNb–NGR-*x* (*x* = 1, 3, 5, 7).

**Table 1** Pore structure parameters of the MNb and MNb-NGR-*x* samples<sup>a</sup>

Sample	$S_{\text{BET}}$ (m <sup>2</sup> g <sup>-1</sup> )	$V_{\text{T}}$ (cm <sup>3</sup> g <sup>-1</sup> )	$D_{\text{BJH}}$ (nm)	NGR (wt%)
MNb	226.2	0.554	7.456	—
MNb-NGR-1	235.3	0.561	7.471	0.76
MNb-NGR-3	242.5	0.568	7.493	2.78
MNb-NGR-5	251.7	0.578	7.542	4.81
MNb-NGR-7	257.6	0.571	7.593	6.85

<sup>a</sup>  $S_{\text{BET}}$  is the specific surface area deduced from the isotherm analysis in the relative pressure range of 0.05–0.35;  $V_{\text{T}}$  is the total pore volume at a relative pressure of 0.95;  $D_{\text{BJH}}$  is the average pore diameter calculated from the adsorption branch of the isotherm using the BJH method.

matching well with the pore diameter distribution from BET measurements. From an HRTEM image of the MNb-NGR-5 composite, shown in Fig. 3e, a lattice fringe spacing of 0.363 nm was measured, and was assigned to the (110) facet of MNb.<sup>38,39</sup> An analysis of the chemical composition of the MNb-NGR-5 composite was also conducted by performing EDX spectroscopy (Fig. 3f). The resulting spectrum indicated the presence of Nb, O, N and C elements in the composites.

The XPS technique was employed to further analyze of chemical composition and the surface electronic states of the

samples. Fig. 4a shows the acquired survey spectra of the MNb and MNb-NGR-5 samples. According to these data, both Nb and O elements were present in these samples, but N was only in the MNb-NGR-5 sample. This result indicated that MNb had successfully combined with N-doped graphene in the MNb-NGR composites. The concentration of NGR in the MNb-NGR-5 sample was found to be 4.81 wt% based on the XPS data (Table 1).<sup>40</sup> Fig. 4b shows magnified views of the Nb 3d regions of the XPS spectra of the MNb and MNb-NGR-5 samples. The MNb sample yielded here two strong peaks, one located at 206.7 eV and the other at 209.5 eV, corresponding to Nb 3d<sub>5/2</sub> and 3d<sub>3/2</sub> states, respectively. Notably, introducing NGR to form MNb-NGR-5 resulted in the Nb 3d<sub>5/2</sub> and Nb 3d<sub>3/2</sub> peaks having shifted to 207.8 and 210.8 eV, which was mainly due to the formation of Nb–O–C bonds between NGR and MNb. A magnified view of the O 1s region of the MNb-NGR-5 sample spectrum is depicted in Fig. 4c; here, deconvolution produced two peaks, one centered at 530.9 eV and the other at 532.4 eV, which corresponded to O–Nb and O–C bonding configurations, respectively.<sup>41</sup> The N 1s region of the XPS spectrum of the MNb-NGR-5 sample is shown in Fig. 4d. Here, deconvoluted peaks were observed at about 399.7 and 400.7 eV, which were attributed to C–N and C=N bonds.<sup>11</sup> Another peak was detected at 398.1 eV, which has been previously described to result from N atoms replacing O atoms in the MNb crystal lattice to form N–Nb–N bonds.<sup>32,42</sup>

The optical properties of pure MNb and MNb-NGR-*x* samples were investigated by performing UV-visible diffuse reflectance spectroscopy. As shown in Fig. 5, the onset of absorption edge gradually shifted to longer wavelengths as the NGR content in the samples was increased.<sup>43</sup> This absorption of longer wavelength by the MNb-NGR-*x* samples was due to the interaction between MNb and NGR, which was also demonstrated from XRD, Raman, and XPS investigations. In

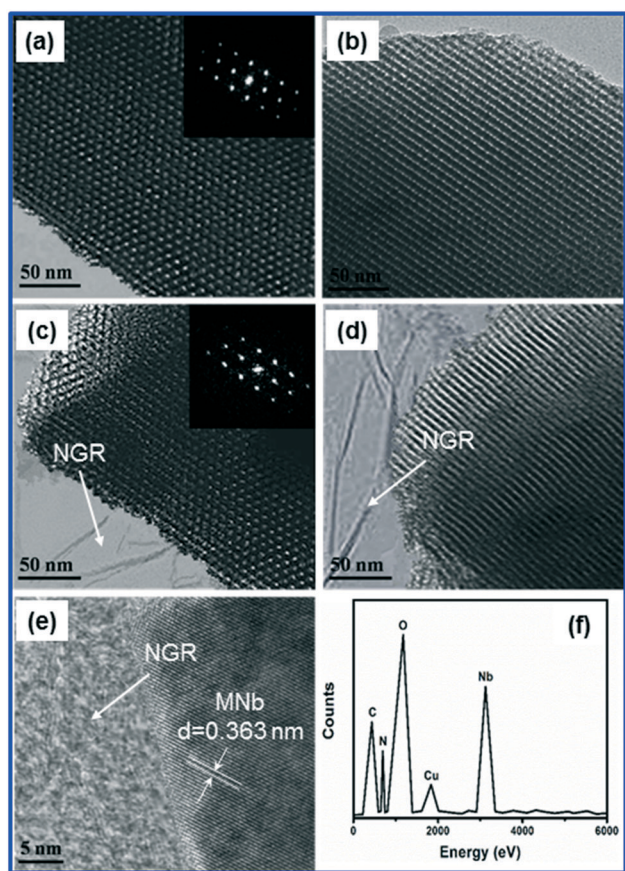


**Fig. 3** (a–d) TEM images of (a and b) MNb and (c and d) MNb-NGR. (e) HRTEM image of MNb-NGR. (f) EDX spectrum of the MNb-NGR composite.

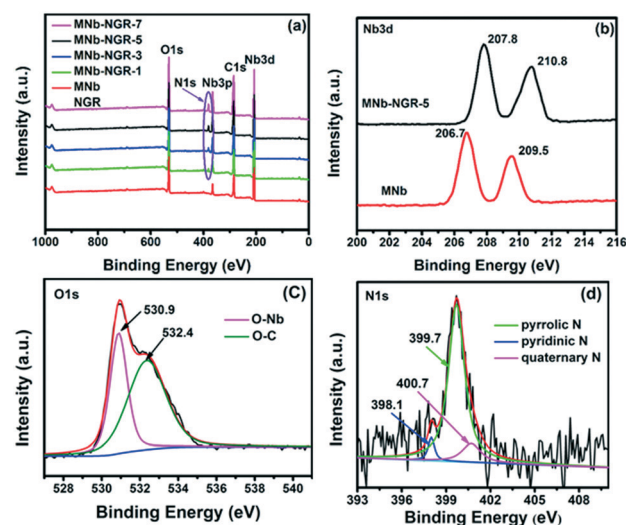


**Fig. 4** (a) XPS survey spectra of MNb and MNb-NGR-*x* (*x* = 1, 3, 5, 7). (b) Nb 3d spectra of MNb and MNb-NGR-5. (c) O 1s spectrum and (d) N 1s spectrum of MNb-NGR-5.

addition, as illustrated in Fig. 5b, the bandgap energies of pure MNb and the MNb-NGR-5 sample were calculated to be about 3.12, and 2.67 eV, respectively, which may have been due to the interaction between MNb and NGR during the recombination process. Therefore, the absorption performance of the photocatalyst in the visible-light region could be directly changed by the binding of MNb to NGR.<sup>44,45</sup>

The above results suggested that the photocatalytic activity of MNb was improved by the introduction of NGR. To investigate the charge separation efficiencies in the MNb-NGR composites, photoluminescence (PL) together with photocurrent response were carried out. First, PL spectra of the various samples were acquired using an excitation wavelength of 400 nm. As shown in Fig. 6a, pure MNb yielded a PL emission peak at about 570 nm. For the MNb-NGR-*x* samples, the intensity of this peak decreased as more NGR was introduced up to an *x* value of 5, but then from this minimum increased a little bit when *x* was increased further to 7. This PL intensity quenching suggested that introduced NGR promoted an efficient separation of charge carriers in the MNb,<sup>46</sup> because the photogenerated electrons in the conduction band (CB) of MNb can be transferred to NGR sheets rapidly. In addition, MNb-NGR-5 displayed the highest quenching efficiency, and further increasing the amount of NGR resulted in a lower quench efficiency. This result was mainly attributed to excessive NGR shielding the light-harvesting properties of MNb, which in general are responsible for the generation of photo-induced electron-hole pairs.<sup>44</sup>

To investigate the electron transfer in the MNb-NGR-*x* samples, we carried out photocurrent response experiments in which the visible light was repeatedly turned on and off. As shown in Fig. 6b, as the relative amount of NGR in the composite increased from 1% to 5 wt%, the photocurrent density gradually increased from 7.7 to 34.4  $\mu\text{A cm}^{-2}$ . Surprisingly, the maximum photocurrent density of MNb-NGR-5 was *ca.* 8.2 times that of the pure MNb-modified electrode under the same conditions, indicating a higher separation efficiency of photoinduced electron-holes in these hybrids. The composite consisting of even more NGR (7 wt%) showed a somewhat lower photocurrent density than did that with 5 wt%, which may have been due to excessive NGR in the composite having blocked some light absorption, leading to a deterioration of the photocatalytic performance.<sup>44</sup> Similar re-

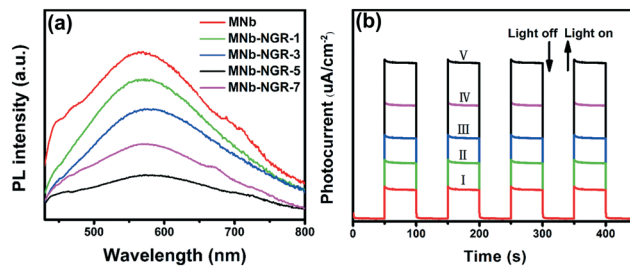


Fig. 6 (a) Photoluminescence spectra of MNb and MNb-NGR-*x* at  $\lambda_{\text{exc}} = 400$  nm. (b) The photocurrent responses of MNb and MNb-NGR-*x* (*x* = 1, 3, 5, 7) to light irradiation recorded at 0.5 V, where the illumination was interrupted every 50 s.

sults were also reported previously.<sup>43,47</sup> In the current work, pure MNb showed a slight photo-activity under visible-light irradiation. This slight activity was attributed to the approximately 3.12 eV bandgap and hence approximately 397 nm absorption edge of the as-prepared MNb. On the other hand, we used in our experiments a filter that cut off wavelengths of light below  $400 \pm 10$  nm. Accordingly, the MNb showed weak activity under visible-light irradiation ( $\lambda > 400$  nm).

Accordingly, the levels of photocatalytic  $\text{H}_2$  production (as a result of the decomposition of water) using the as-prepared samples under irradiation with visible light are shown in Fig. 7a. After 5 h of such illumination, while almost no  $\text{H}_2$  was detected when bulk  $\text{Nb}_2\text{O}_5$  or MNb was used as the photocatalyst, when instead using the MNb-NGR-1 composite, the amount of  $\text{H}_2$  evolved was  $12.5 \mu\text{mol g}^{-1}$ . And from this level, the amount of  $\text{H}_2$  that evolved then increased 3.9 fold, to  $49.2 \mu\text{mol g}^{-1}$ , as the relative amount of NGR in the MNb-NGR sample was increased to 5 wt%, but then decreased when the amount of NGR was increased further to 7 wt%. These results demonstrated a considerable acceleration

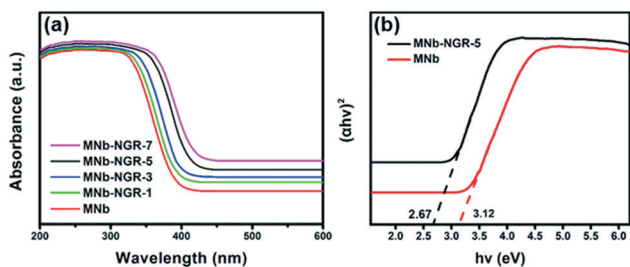


Fig. 5 (a) UV-vis diffuse reflectance spectra of MNb and MNb-NGR-*x* (*x* = 1, 3, 5, 7). (b)  $\mu$  plots of  $(\alpha hv)^2$  versus energy  $hv$  for MNb and MNb-NGR-5.

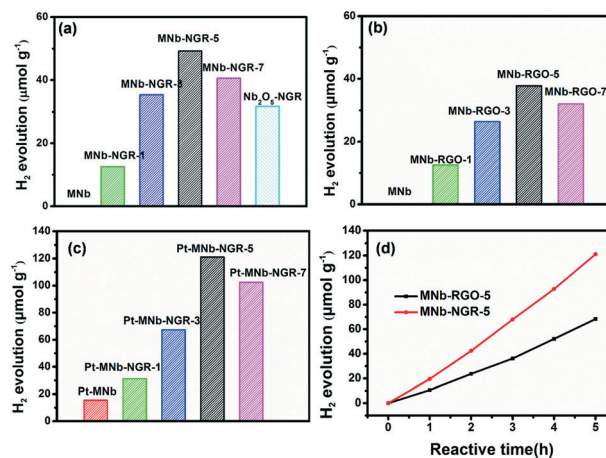


Fig. 7 (a-c) The amounts of  $\text{H}_2$  evolved after 5 h of visible-light illumination using (a) MNb-NGR-*x*, (b) MNb-RGO-*x*, and (c) Pt(0.5 wt%)-MNb-NGR-*x* composites, and (d)  $\text{H}_2$  evolution as a function of reaction time for the MNb-NGR-5 and MNb-RGO-5 samples. Reaction conditions:  $m_{\text{catalyst}} = 25$  mg,  $\text{pH} = 7$ ,  $T = 298$  K, source of visible light: 150 W Xe lamp with a cut-off filter ( $\lambda > 400$  nm).

of the  $\text{H}_2$  evolution rate as a result of using NGR with large surface areas and excellent electronic conductivity. Therefore, the combination of MNb with NGR was concluded to give rise to a synergistic effect on the photocatalytic activity for the  $\text{H}_2$  evolution, and NGR may be used effectively as a solid-state electron mediator to facilitate charge transfer, separation, and thus improve the separation efficiency of photogenerated electrons and holes. We also used non-porous  $\text{Nb}_2\text{O}_5$  particles to decorate NGR, and a considerable amount ( $31.7 \mu\text{mol g}^{-1}$ ) of  $\text{H}_2$  was detected after 5 h of visible-light illumination. As shown in Fig. 7b, a similar experiment was conducted but using RGO substituting for NGR under the same conditions. (A TEM image of MNb-RGO-5 is shown in Fig. S2†). After 5 h of reaction, the amount of  $\text{H}_2$  evolved increased to  $37.8 \mu\text{mol g}^{-1}$  as the amount of RGO doped on the MNb was increased from 1 to 5 wt% (MNb-RGO-5), and then decreased to  $32.1 \mu\text{mol g}^{-1}$  at higher RGO doping (MNb-RGO-7). Obviously, the enhanced photocatalytic activity could be attributed to the larger specific surface area of MNb-RGO composites and the good interfacial contacts between well-ordered MNb and RGO.<sup>36</sup>

The effect of the Pt(0.5 wt%) loading on the amount of  $\text{H}_2$  evolved when using MNb-NGR catalysts is shown in Fig. 7c. First, the amount of  $\text{H}_2$  evolved (again as a result of the decomposition of water) was observed to be  $15.5 \mu\text{mol g}^{-1}$  of MNb under visible-light irradiation for 5 h. When the NGR was introduced, the catalytic activity improved, and increased with the increase of the weight ratio of NGR from 1% to 5%. The optimal weight ratio of NGR in the composites of MNb-NGR-x was found to be 5% where the amount of  $\text{H}_2$  reached  $121.1 \mu\text{mol g}^{-1}$ , *ca.* 7.8 times that of MNb. Such enhanced photocatalytic performance was attributed to the superior interfacial contacts between MNb and NGR, which can offer more active sites during a photocatalytic reaction, and to NGR being able to act as an excellent electronic transmission medium to accelerate the separation of photogenerated charge carriers. However, upon further increasing the relative amount of NGR, the  $\text{H}_2$  yield decreased (to  $102.4 \mu\text{mol g}^{-1}$ ), due to the excessive amounts of NGR causing a detrimental effect on the absorption of visible light.<sup>44,48</sup>

The pronounced photocatalytic activity of MNb-NGR-x could be explained by considering the synergistic effect of including both MNb and NGR. As shown in Fig. 7d, MNb-NGR-5 displayed a higher photocatalytic activity than did MNb-RGO-5 ( $68.3 \mu\text{mol g}^{-1}$ ), with this difference mostly due to the better electrical conductivity of NGR as well as nitrogen atoms in NGR acting as nucleation and anchor sites for MNb on NGR.<sup>28,49</sup> We concluded that the intimate interfacial contact between MNb and NGR played a major role in increasing the photocatalytic performance, and nitrogen from MNb-NGR-5 also bridged such integration and thus synergistically improved the efficiency of the photoinduced charge transfer and separation.<sup>42</sup>

The stability of a photocatalyst material is an important property to evaluate. The stability of a MNb-NGR-5 sample for photocatalytic  $\text{H}_2$  evolution was evaluated by testing its photo-

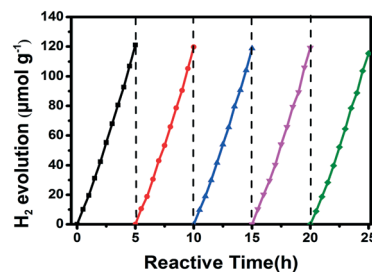


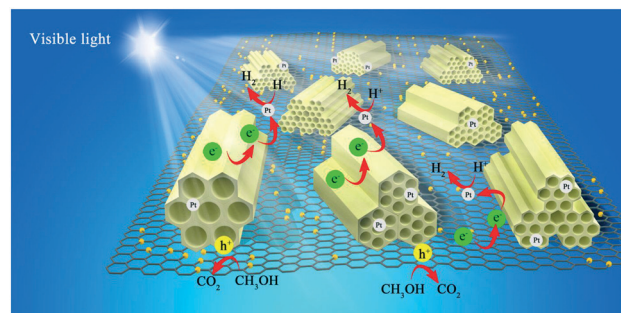
Fig. 8 Recycling study of the MNb-NGR-5 photocatalyst for  $\text{H}_2$  evolution.

catalytic performance over the course of five cycles of use, as shown in Fig. 8. Its photocatalytic activity displayed a negligible decrease after five such cycles, which showed the good stability and durability of the MNb-NGR-5 sample for photocatalytic  $\text{H}_2$  evolution under irradiation with visible light.

Based on the above analyses, we derived a mechanism, shown in Scheme 1, for the photocatalytic production of  $\text{H}_2$  using the MNb-NGR sample under visible-light irradiation. According to this model, such irradiation resulted in a transfer of electrons ( $e^-$ ) from the valence band (VB) to the CB of MNb and then to Pt nanoparticles loaded on the NGR nanosheets used as a co-catalyst of the reduction of protons and hence production of  $\text{H}_2$ . This process was, according to the model, facilitated by the relatively high number of electron traps in MNb and the superior interfacial contacts between MNb and NGR.<sup>37</sup> Meanwhile, the holes remained on the surface of MNb to oxidize  $\text{CH}_3\text{OH}$  to  $\text{CO}_2$ . As a result, both the surface and textural structures of MNb were tailored to provide a short diffusion pathway for photogenerated electron transport and, depending on N doping, introduced NGR acted as nucleation and anchor sites to synergistically accelerate the migration of photogenerated electrons on the catalyst surface, leading to a promotion of hydrogen production under visible-light irradiation.

### 3. Conclusions

In conclusion, a new nanocomposite made of a highly ordered mesoporous structure of  $\text{Nb}_2\text{O}_5$  arrays combined with



Scheme 1 Schematic illustration of the transfer of photoexcited electrons and production of  $\text{H}_2$  catalyzed by MNb-NGR under visible-light illumination.

N-doped graphene was successfully synthesized using the sample sol-gel method. Importantly, the as-synthesized MNb-NGR composites exhibited effective interfacial contact between MNb and NGR, contributing to a 7.8 times greater photocatalytic H<sub>2</sub> production under visible-light illumination than that observed using pure MNb. The enhancement of photocatalytic performance can be attributed to MNb with a highly ordered mesostructure providing more reaction sites and a direct path for photoinduced charge transfer, and due to N doping from introduced NGR, which acted as nucleation and anchor sites that synergistically enhanced electron transfer between MNb and NGR and thus efficiently suppressed the recombination of electron-hole pairs. This study opens up a new way to fabricate the MNb-NGR hybrid as a promising candidate for solar energy conversion.

## 4. Experimental

### 4.1 Materials

The block copolymer surfactant EO<sub>106</sub>PO<sub>70</sub>EO<sub>106</sub> (Sigma-Aldrich, F127, MW: 12600), niobium chloride (J&K, NbCl<sub>5</sub>), anhydrous ethanol, anhydrous calcium chloride (CaCl<sub>2</sub>), urea, graphene, hydrochloric acid (HCl), H<sub>2</sub>PtCl<sub>6</sub> (Alfa Aesar), and methanol were obtained and used directly.

### 4.2 Synthesis of the composite of highly ordered mesoporous Nb<sub>2</sub>O<sub>5</sub> arrays on N-doped graphene

First, N-doped graphene (NGR) was synthesized by carrying out a solid-state thermal reaction method. A mass of 0.5 g of graphene and a mass of 1.5 g of urea were ground to a sufficient extent, and placed in a tube furnace. Under inert gas ambient, the temperature of the furnace was raised from room temperature to 1323 K at a heating rate of 5 °C min<sup>-1</sup>, and then calcined at the indicated temperature for 10 h. The samples were then washed several times using 1 M hydrochloric acid to remove impurities. Finally, the samples were dried in an oven at 60 °C overnight, and as a result, N-doped graphene was obtained.

The highly ordered mesoporous Nb<sub>2</sub>O<sub>5</sub> (MNb) was synthesized by using a sol-gel method.<sup>17</sup> A mass of 1 g of F127 was dissolved into 20 mL of ethanol with vigorous stirring for 10 min. Then, 5.5 mmol of NbCl<sub>5</sub> was added into the above solution with stirring for 30 min. After that, a volume of 0.5 mL of water was added into the above dispersion and with further stirring for 10 min. Finally, the generated sol was transferred into a Teflon-coated autoclave and heated at 70 °C for 7 days. After this reaction, the aged gel samples were washed with ethanol thoroughly and then dried at 40 °C overnight. For removal of surfactant, the samples were calcined at 450 °C for 5 h in air, resulting in highly ordered mesoporous Nb<sub>2</sub>O<sub>5</sub>.

The composite of highly ordered mesoporous Nb<sub>2</sub>O<sub>5</sub> arrays on N-doped graphene was synthesized by carrying out a roasting method. In a typical experiment, a mass of 0.1 g of the as-obtained MNb sample was finely milled with various amounts of NGR and then transferred into a covered crucible

and heated at 450 °C for 4 h under an argon atmosphere. The resulting samples were labeled as MNb-NGR-*x* (with *x* representing the percent weight ratio of MNb:NGR, *x* = 1, 3, 5 and 7).

### 4.3 Photocatalytic H<sub>2</sub> evolution

The photocatalytic H<sub>2</sub> reactions were performed in a closed gas circulation system. First, 20 mg of samples were dispersed into an aqueous methanol solution (70 mL distilled H<sub>2</sub>O, 10 mL CH<sub>3</sub>OH) in an inner irradiation quartz cell under stirring. Using the *in situ* photodeposition method, cocatalyst Pt nanoparticles were decorated on the surface of the photocatalyst.<sup>17</sup> In detail, 50 μL of an aqueous solution of 0.04 M H<sub>2</sub>PtCl<sub>6</sub> were added into the above system and then the system was deaerated by bubbling argon into the solution for 30 min before the light irradiation. The mixed solution was irradiated by using a GY-10 xenon lamp (150 W) with a cut-off filter ( $\lambda > 400 \pm 10$  nm). The gases were analyzed by using a gas chromatograph (GC, Varian CP3800) with a thermal conductivity detector (TCD).

### 4.4 Characterizations

The morphologies of the samples were observed by using a transmission electron microscopy (TEM, Philips TECNAI-12) instrument. Energy-dispersive X-ray (EDX) analysis was conducted using a KEVEX X-ray energy detector. The porosity properties of all of the samples were investigated by acquiring N<sub>2</sub> adsorption-desorption isotherms (BET) at 77 K. X-ray diffraction (XRD) patterns of samples were acquired in the range of 1–3° for small-angle XRD and 10–80° for wide-angle XRD by using a Philips diffractometer together with Ni-filtered Cu K $\alpha$  radiation. The optical properties of the samples were determined using a UV-1800 SPC spectrophotometer to obtain UV-vis diffuse reflectance spectra (DRS). The samples for X-ray photoelectron spectroscopy (XPS) were obtained by dropping a dilute colloidal dispersion onto the surface of a silicon wafer and then dried in air. The XPS experiments were performed on an AXIS Ultra DLD system (Kratos Analytical Inc.) with monochromatic Al K $\alpha$  radiation. Photoelectrochemical measurements of the samples were taken in a three-electrode system consisting of an indium tin oxide (ITO) glass covered with the sample, a platinum (Pt) wire, and an Ag/AgCl electrode on a CHI 660B electrochemical analyzer. The ITO covered the sample, Pt wire, and Ag/AgCl electrode served as the working electrode, counter electrode, and reference electrode, respectively. All experiments were carried out at room temperature.

## Conflicts of interest

There are no conflicts to declare.

## Acknowledgements

This work was financially supported by National Natural Science Foundation of China (Grant No. 21603111), Jiangsu

province fourth issue of “333 High-level Talents Training Project” (Grant No. BRA2015120, BRA2016202), Application Research Program of Nantong (Grant No. GY12016050, MS12015028, JC2018013, JC2018071) and Qing Lan Project of Jiangsu Province.

## Notes and references

- C. Kresge, M. Leonowicz, W. Roth, J. Vartuli and J. Beck, *Nature*, 1992, **359**, 710–712.
- T. Yanagisawa, T. Shimizu, K. Kuroda and C. Kato, *Bull. Chem. Soc. Jpn.*, 1990, **63**, 988–992.
- Y. Shi, Y. Wan and D. Zhao, *Chem. Soc. Rev.*, 2011, **40**, 3854–3878.
- Y. Ren, Z. Ma and P. Bruce, *Chem. Soc. Rev.*, 2012, **41**, 4909–4927.
- S. Wang, *Microporous Mesoporous Mater.*, 2009, **117**, 1–9.
- A. Taguchi and F. Schüth, *Microporous Mesoporous Mater.*, 2005, **77**, 1–45.
- F. Xiao, Y. Han, Y. Yu, X. Meng, M. Yang and S. Wu, *J. Am. Chem. Soc.*, 2002, **124**, 888–889.
- J. Rosen, G. Hutchings and F. Jiao, *J. Am. Chem. Soc.*, 2013, **135**, 4516–4521.
- W. Zhou, W. Li, J. Wang, Y. Qu and D. Zhao, *J. Am. Chem. Soc.*, 2014, **136**, 9280–9283.
- A. Prado, L. Bolzon, C. Pedroso, A. Moura and L. Costa, *Appl. Catal., B*, 2008, **82**, 219–224.
- X. Chen, T. Yu, X. Fan, H. Zhang, Z. Li, J. Ye and Z. Zou, *Appl. Surf. Sci.*, 2007, **253**, 8500–8506.
- M. Wu, X. Lin, W. Guo, Y. Wang, L. Chu, T. Ma and K. Wu, *Chem. Commun.*, 2013, **49**, 1058–1060.
- R. Rani, A. Zoolfakar, J. Ou, M. Field, M. Austin and K. Kalantar-Zadeh, *Sens. Actuators, B*, 2013, **176**, 149–156.
- E. Lim, H. Kim, C. Jo, J. Chun and J. Lee, *ACS Nano*, 2014, **8**, 8968–8978.
- C. Kao, H. Chen, L. Kuo, J. Wang, Y. Chen, Y. Chu, C. Chen, C. Lai, S. Chang and C. Chang, *Sens. Actuators, B*, 2014, **194**, 419–426.
- M. Qamar, M. Abdalwadoud, M. Ahmed, A. Azad, B. Merzougui, S. Bukola, Z. Yamani and M. Siddiqui, *ACS Appl. Mater. Interfaces*, 2015, **7**, 17954–17962.
- H. Huang, C. Wang, J. Huang, X. Wang, Y. Du and P. Yang, *Nanoscale*, 2014, **6**, 7274–7280.
- O. Lopes, E. Paris and C. Ribeiro, *Appl. Catal., B*, 2014, **144**, 800–808.
- Y. Zhao, X. Zhou, L. Ye and E. Tsang, *Nano Rev.*, 2012, **3**, 17631.
- S. Ge, H. Jia, H. Zhao, Z. Zheng and L. Zhang, *J. Mater. Chem.*, 2010, **20**, 3052–3058.
- D. Wei, Y. Liu, Y. Wang, H. Zhang, L. Huang and G. Yu, *Nano Lett.*, 2009, **9**, 1752–1758.
- L. Panchakarla, K. Subrahmanyam, S. Saha, A. Govindaraj, H. Krishnamurthy, U. Waghmare and C. Rao, *Adv. Mater.*, 2009, **21**, 4726–4730.
- H. Li, S. Gan, H. Wang, D. Han and L. Niu, *Adv. Mater.*, 2015, **27**, 6906–6913.
- Y. Hou, Z. Wen, S. Cui, X. Guo and J. Chen, *Adv. Mater.*, 2013, **25**, 6291–6297.
- T. Yeh, C. Teng, S. Chen and T. Hsisheng, *Adv. Mater.*, 2014, **26**, 3297–3303.
- Y. Lei, Q. Shi, C. Han, B. Wang, N. Wu, H. Wang and Y. Wang, *Nano Res.*, 2016, **9**, 2498–2509.
- W. Ong, L. Tan, S. Chai, S. Yong and A. Mohamed, *Nano Res.*, 2014, **7**, 1528–1547.
- D. Chang and J. Baek, *Chem. – Asian J.*, 2016, **11**, 1125–1137.
- M. Zhu, Y. Lu, Y. Du, J. Li, X. Wang and P. Yang, *Int. J. Hydrogen Energy*, 2011, **36**, 4298–4304.
- L. Kong, C. Zhang, J. Wang, W. Qiao, L. Ling and D. Long, *ACS Nano*, 2015, **9**, 11200–11208.
- F. Sun, H. Cheng, J. Chen, N. Zheng, Y. Li and J. Shi, *ACS Nano*, 2016, **10**, 8289–8298.
- S. Shin, J. Park, K. Kim, K. Choi and J. Kang, *Chem. Mater.*, 2016, **28**, 7725–7730.
- Y. Shen, T. Xiong, J. Shang and K. Yang, *Res. Chem. Intermed.*, 2008, **34**, 353–363.
- Y. Zhang, J. Tian, H. Li, L. Wang, X. Qin, A. Asiri, A. Al-Youbi and X. Sun, *Langmuir*, 2012, **28**, 12893–12900.
- G. Zhao, X. Huang, X. Wang, P. Connor, J. Li, S. Zhang and J. Irvine, *J. Mater. Chem. A*, 2015, **3**, 297–303.
- Z. Yue, A. Liu, C. Zhang, J. Huang, M. Zhu, Y. Du and P. Yang, *Appl. Catal., B*, 2017, **201**, 202–210.
- J. Wei, Y. Li, M. Wang, Q. Yue, Z. Sun, C. Wang, Y. Zhao, Y. Deng and D. Zhao, *J. Mater. Chem. A*, 2013, **1**, 8819–8827.
- H. Huang, Z. Yue, G. Li, X. Wang, J. Huang, Y. Du and P. Yang, *J. Mater. Chem. A*, 2014, **2**, 20118–20125.
- H. Shibata, T. Ogura, T. Mukai, T. Ohkubo, H. Sakai and M. Abe, *J. Am. Chem. Soc.*, 2005, **127**, 16396–16397.
- G. Yang, Z. Jiang, H. Shi, T. Xiao and Z. Yan, *J. Mater. Chem.*, 2010, **20**, 5301–5309.
- S. Yang, X. Song, P. Zhang and L. Gao, *ACS Appl. Mater. Interfaces*, 2013, **5**, 3317–3322.
- Y. Wu, D. Chu, P. Yang, Y. Du and C. Lu, *Catal. Sci. Technol.*, 2015, **5**, 3375–3382.
- J. Zhang, J. Yu, M. Jaroniec and J. Gong, *Nano Lett.*, 2012, **12**, 4584–4589.
- Q. Li, B. Guo, J. Yu, J. Ran and J. Gong, *J. Am. Chem. Soc.*, 2011, **133**, 10878–10884.
- J. Xu, L. Luo, G. Xiao, Z. Zhang, H. Lin, X. Wang and J. Long, *ACS Catal.*, 2014, **4**, 3302–3306.
- Q. Huang, S. Tian, D. Zeng, X. Wang, W. Song, Y. Li, W. Xiao and C. Xie, *ACS Catal.*, 2013, **3**, 1477–1485.
- H. Huang, Z. Yue, G. Li, X. Wang, J. Huang, Y. Du and P. Yang, *J. Mater. Chem. A*, 2013, **1**, 15110–15116.
- A. Mukherji, B. Seger, G. Lu and L. Wang, *ACS Nano*, 2011, **5**, 3483–3492.
- Z. Mou, Y. Wu, J. Sun, P. Yang, Y. Du and C. Lu, *ACS Appl. Mater. Interfaces*, 2014, **6**, 13798–13806.